Title
Near-concentric Fabry-Pérot cavity for continuous-wave laser control of electron waves.

Journal
Optics express, 25(13)

ISSN
1094-4087

Authors
Schwartz, O
Axelrod, JJ
Tuthill, DR
et al.

Publication Date
2017-06-01

DOI
10.1364/oe.25.014453

Peer reviewed

Research Article | Vol. 25, No. 13 | 26 Jun 2017 | OPTICS EXPRESS 14453
Optics EXPRESS

Near-concentric Fabry-Pérot cavity for continuous-wave laser control of electron waves

O. SCHWARTZ,[1,*] J. J. AXELROD,[1] D. R. TUTHILL,[1] P. HASLINGER,[1] C. OPHUS,[2] R. M. GLAESER,[3,4] AND H. MÜLLER[1,3]

[1]*Physics Department, University of California, Berkeley, California, USA*
[2]*National Center for Electron Microscopy, Molecular Foundry, Lawrence Berkeley National Laboratory, Berkeley, California, USA*
[3]*Lawrence Berkeley National Laboratory, Berkeley, California, USA*
[4]*Molecular and Cell Biology Department, University of California, Berkeley, California, USA*
[*]*osip@berkeley.edu*

Abstract: Manipulating free-space electron wave functions with laser fields can bring about new electron-optical elements for transmission electron microscopy (TEM). In particular, a Zernike phase plate would enable high-contrast TEM imaging of soft matter, leading to new opportunities in structural biology and materials science. A Zernike phase plate can be implemented using a tight, intense continuous laser focus that shifts the phase of the electron wave by the ponderomotive potential. Here, we use a near-concentric cavity to focus 7.5 kW of continuous-wave circulating laser power at 1064 nm into a 7 μm mode waist, achieving a record continuous laser intensity of 40 GW/cm^2. Such parameters are sufficient to impart a phase shift of 1 rad to a 10 keV electron beam, or 0.16 rad to a 300 keV beam. Our numerical simulations confirm that the standing-wave phase shift profile imprinted on the electron wave by the intra-cavity field can serve as a nearly ideal Zernike phase plate.

OCIS codes: (110.0180) Microscopy; (140.4780) Optical resonators; (170.0110) Imaging systems; (020.2649) Strong field laser physics.

References and links

1. J. C. H. Spence, *High-Resolution Electron Microscopy* (Oxford University, 2013).
2. G. Möllenstedt and H. Düker, "Beobachtungen und Messungen an Biprisma-Interferenzen mit Elektronenwellen," Zeitschrift für Physik **145**, 377–397 (1956).
3. A. Tonomura, "Applications of electron holography," Rev. Modern Phys. **59**, 639–669 (1987).
4. P. A. Midgley and R. E. Dunin-Borkowski, "Electron tomography and holography in materials science," Nat. Mater. **8**, 271–280 (2009).
5. B. J. McMorran, A. Agrawal, I. M. Anderson, A. A. Herzing, H. J. Lezec, J. J. McClelland, and J. Unguris, "Electron Vortex Beams with High Quanta of Orbital Angular Momentum," Science **331**, 192–195 (2011).
6. V. Grillo, G. C. Gazzadi, E. Mafakheri, S. Frabboni, E. Karimi, and R. W. Boyd, "Holographic Generation of Highly Twisted Electron Beams," Phys. Rev. Lett. **114**, 034801 (2015).
7. J. Verbeeck, H. Tian, and P. Schattschneider, "Production and application of electron vortex beams," Nature **467**, 301–304 (2010).
8. R. M. Glaeser, "Invited Review Article: Methods for imaging weak-phase objects in electron microscopy," Rev. Sci. Instrum. **84**, 111101 (2013).
9. E. Jones, M. Becker, J. Luiten, and H. Batelaan, "Laser control of electron matter waves," Laser Photonics Rev. **10**, 214–229 (2016).
10. W. E. King, G. H. Campbell, A. Frank, B. Reed, J. F. Schmerge, B. J. Siwick, B. C. Stuart, and P. M. Weber, "Ultrafast electron microscopy in materials science, biology, and chemistry," J. Appl. Phys. **97**, 111101 (2005).
11. P. Baum, D.-S. Yang, and A. H. Zewail, "4d Visualization of Transitional Structures in Phase Transformations by Electron Diffraction," Science **318**, 788–792 (2007).
12. J. Breuer and P. Hommelhoff, "Laser-Based Acceleration of Nonrelativistic Electrons at a Dielectric Structure," Phys. Rev. Lett. **111**, 134803 (2013).
13. A. Feist, K. E. Echternkamp, J. Schauss, S. V. Yalunin, S. Schäfer, and C. Ropers, "Quantum coherent optical phase modulation in an ultrafast transmission electron microscope," Nature **521**, 200–203 (2015).
14. A. Howie, "Photon interactions for electron microscopy applications," Eur. Phys. J. Appl. Phys. **54**, 33502 (2011).
15. D. L. Freimund, K. Aflatooni, and H. Batelaan, "Observation of the Kapitza-Dirac effect," Nature **413**, 142–143 (2001).

https://doi.org/10.1364/OE.25.014453 https://doi.org/10.1364/OE.25.014453
Journal © 2017 Received 2 Mar 2017; revised 1 Jun 2017; accepted 2 Jun 2017; published 16 Jun 2017

Optics EXPRESS

16. D. L. Freimund and H. Batelaan, "Bragg Scattering of Free Electrons Using the Kapitza-Dirac Effect," Phys. Rev. Lett. **89**, 283602 (2002).
17. J. Handali, P. Shakya, and B. Barwick, "Creating electron vortex beams with light," Opt. Express **23**, 5236–5243 (2015).
18. H. Müller, J. Jin, R. Danev, J. Spence, H. Padmore, and R. M. Glaeser, "Design of an electron microscope phase plate using a focused continuous-wave laser," New J. Phys. **12**, 073011 (2010).
19. E. Nogales, "The development of cryo-EM into a mainstream structural biology technique," Nat. Methods **13**, 24–27 (2016).
20. R. M. Glaeser, "How good can cryo-EM become?" Nat. Methods **13**, 28–32 (2016).
21. E. Callaway, "The revolution will not be crystallized: a new method sweeps through structural biology," Nature **525**, 172–174 (2015).
22. R. Glaeser, K. Downing, D. DeRosier, W. Chiu, and J. Frank, *Electron Crystallography of Biological Macromolecules*, 1st ed. (Oxford University, 2007).
23. R. Henderson, "The potential and limitations of neutrons, electrons and X-rays for atomic resolution microscopy of unstained biological molecules," Quarterly Rev. Biophys. **28**, 171–193 (1995).
24. S. Asano, Y. Fukuda, F. Beck, A. Aufderheide, F. Förster, R. Danev, and W. Baumeister, "A molecular census of 26s proteasomes in intact neurons," Science **347**, 439–442 (2015).
25. R. Danev, B. Buijsse, M. Khoshouei, J. M. Plitzko, and W. Baumeister, "Volta potential phase plate for in-focus phase contrast transmission electron microscopy," Proc. Natl. Acad. Sci. **111**, 15635–15640 (2014).
26. W. Dai, C. Fu, D. Raytcheva, J. Flanagan, H. A. Khant, X. Liu, R. H. Rochat, C. Haase-Pettingell, J. Piret, S. J. Ludtke, K. Nagayama, M. F. Schmid, J. A. King, and W. Chiu, "Visualizing virus assembly intermediates inside marine cyanobacteria," Nature **502**, 707–710 (2013).
27. H. Batelaan, "Illuminating the Kapitza-Dirac effect with electron matter optics," Rev. Mod. Phys. **79**, 929–941 (2007).
28. J. Park, H. Elmlund, P. Ercius, J. M. Yuk, D. T. Limmer, Q. Chen, K. Kim, S. H. Han, D. A. Weitz, A. Zettl, and A. P. Alivisatos, "3d structure of individual nanocrystals in solution by electron microscopy," Science **349**, 290–295 (2015).
29. W. J. Huang, J. M. Zuo, B. Jiang, K. W. Kwon, and M. Shim, "Sub-ångström-resolution diffractive imaging of single nanocrystals," Nat. Phys. **5**, 129–133 (2009).
30. L. S. Meng, J. K. Brasseur, and D. K. Neumann, "Damage threshold and surface distortion measurement for high-reflectance, low-loss mirrors to 100+ MW/cm2 cw laser intensity," Opt. Express **13**, 10085 (2005).
31. K. Durak, C. H. Nguyen, V. Leong, S. Straupe, and C. Kurtsiefer, "Diffraction-limited Fabry-Pérot cavity in the near concentric regime," New J. Phys. **16**, 103002 (2014).
32. H. Carstens, N. Lilienfein, S. Holzberger, C. Jocher, T. Eidam, J. Limpert, A. Tünnermann, J. Weitenberg, D. C. Yost, A. Alghamdi, Z. Alahmed, A. Azzeer, A. Apolonski, E. Fill, F. Krausz, and I. Pupeza, "Megawatt-scale average-power ultrashort pulses in an enhancement cavity," Opt. Lett. **39**, 2595 (2014).
33. A. Cingöz, D. C. Yost, T. K. Allison, A. Ruehl, M. E. Fermann, I. Hartl, and J. Ye, "Direct frequency comb spectroscopy in the extreme ultraviolet," Nature **482**, 68–71 (2012).
34. G. Berden, R. Peeters, and G. Meijer, "Cavity ring-down spectroscopy: Experimental schemes and applications," Int. Rev. Phys. Chem. **19**, 565–607 (2000).
35. B. J. Orr and Y. He, "Rapidly swept continuous-wave cavity-ringdown spectroscopy," Chem. Phys. Lett. **512**, 1–20 (2011).
36. M. Khoshouei, M. Radjainia, W. Baumeister, and R. Danev, "Cryo-EM structure of haemoglobin at 3.2 A determined with the Volta phase plate," bioRxiv p. 087841 (2016).
37. E. J. Kirkland, *Advanced Computing in Electron Microscopy*, 2nd ed. (Springer, 2010).
38. J. S. Kavanaugh, W. F. Moo-Penn, and A. Arnone, "Accommodation of insertions in helices: the mutation in hemoglobin Catonsville (Pro 37 alpha-Glu-Thr 38 alpha) generates a 3(10)–>alpha bulge," Biochemistry **32**, 2509–2513 (1993).
39. Z. Shang and F. J. Sigworth, "Hydration layer models for cryo-EM image simulation," J. Structural Biol. **180**, 10–16 (2012).
40. Y. Cheng, "Single-Particle Cryo-EM at Crystallographic Resolution," Cell **161**, 450–457 (2015).
41. A. Merk, A. Bartesaghi, S. Banerjee, V. Falconieri, P. Rao, M. I. Davis, R. Pragani, M. B. Boxer, L. Earl, J. S. Milne, and S. Subramaniam, "Breaking Cryo-EM Resolution Barriers to Facilitate Drug Discovery," Cell **165**, 1698–1707 (2016).
42. P. Kruit, R. G. Hobbs, C.-S. Kim, Y. Yang, V. R. Manfrinato, J. Hammer, S. Thomas, P. Weber, B. Klopfer, C. Kohstall, T. Juffmann, M. A. Kasevich, P. Hommelhoff, and K. K. Berggren, "Designs for a quantum electron microscope," Ultramicroscopy **164**, 31–45 (2016).
43. M. Wolke, J. Klinner, H. Keßler, and A. Hemmerich, "Cavity Cooling Below the Recoil Limit," Science **337**, 75–78 (2012).
44. A. Stute, B. Casabone, P. Schindler, T. Monz, P. O. Schmidt, B. Brandstätter, T. E. Northup, and R. Blatt, "Tunable ion-photon entanglement in an optical cavity," Nature **485**, 482–485 (2012).
45. P. D. Edmunds and P. F. Barker, "A deep optical cavity trap for atoms and molecules with rapid frequency and intensity modulation," Rev. Sci. Instrum. **84**, 083101 (2013).
46. Y.-J. Chen, L. F. Gonçalves, and G. Raithel, "Measurement of Rb $5{P}_{3/2}$ scalar and tensor polarizabilities in

Optics EXPRESS

a 1064-nm light field," Phys. Rev. A **92**, 060501 (2015).
47. D. E. Chang, C. A. Regal, S. B. Papp, D. J. Wilson, J. Ye, O. Painter, H. J. Kimble, and P. Zoller, "Cavity opto-mechanics using an optically levitated nanosphere," Proc. Natl. Acad. Sci. **107**, 1005–1010 (2010).
48. P. Asenbaum, S. Kuhn, S. Nimmrichter, U. Sezer, and M. Arndt, "Cavity cooling of free silicon nanoparticles in high vacuum," Nat. Commun. **4**, 2743 (2013).
49. N. Kiesel, F. Blaser, U. Delić, D. Grass, R. Kaltenbaek, and M. Aspelmeyer, "Cavity cooling of an optically levitated submicron particle," Proc. Natl. Acad. Sci. **110**, 14180–14185 (2013).

1. Introduction

The imaging system of a conventional transmission electron microscope (TEM) is built of just a few highly evolved electron-optical elements, such as the electron gun, magnetic lens, and energy filter [1]. Historically, development of additional electron-optical elements has lead to expanded functionality of TEM. The invention of the charged-filament Fresnel biprism [2] has given rise to the field of electron holography [3, 4]. Nano-fabricated holographic phase plates [5, 6] have been used to produce vortex beams, which enable probing the magnetic properties of materials [7]. A number of electrostatic, magnetic, and thin film-based devices have been used to implement in-focus phase contrast [8].

Controlling free-space electron propagation with lasers offers an alternative approach to electron optics [9]. Ultrafast TEM relies on laser pulses to produce femtosecond electron bursts [10, 11]. Laser fields in the presence of plasmon-carrying structures have been used to accelerate electron beams [12] and to shape the temporal profile of the electron wave function [13]. However, free space electron-laser interaction has not yet been applied, to our knowledge, as a means for coherent spatial control of electron waves in an imaging system.

A charged particle traversing an intense laser field experiences small-scale oscillatory motion, resulting in an effective 'ponderomotive' potential [14]. Various laser field configurations can thus be utilized to implement electron-optical elements. Such laser-based electron optics do not require material objects to be inserted in the electron beam path, and thus are not susceptible to beam-induced damage and offer negligible electron loss, in addition to having controllable potential depth. The ponderomotive potential of a standing laser wave has been used to create a diffraction grating [15] and a Bragg beam splitter [16] for electron beams. A phase plate for creating electron vortex beams can be realized using a standing wave of optical vortex beams [17]. It has also been proposed that a laser beam focused in the back focal plane of a TEM objective lens can serve as a Zernike phase plate [18].

Development of a laser-based Zernike phase plate would be particularly useful for structural biology. Recent technological advances in transmission electron microscopy of frozen-hydrated, unstained specimens (cryo-EM) have made it possible to retrieve the three-dimensional structure of biological macromolecules with near-atomic resolution [19–21]. In conventional cryo-EM, the nearly transparent protein assemblies are made visible by defocusing the imaging system [22]. The drawback of this method is that the low spatial frequency components of the image, essential for identification and classification of the particles, are heavily attenuated. Poor contrast at low spatial frequencies hampers reconstruction of protein complexes with a molecular weight below 100 – 200 kDa, or even larger assemblies that exhibit significant structural variability. On the other hand, cryo-EM reconstruction of particles as small as 40 kDa is theoretically possible with an in-focus phase contrast device, such as a Zernike phase plate [8, 23].

Recently, the capabilities of Zernike phase contrast in cryo-EM have been demonstrated with phase plates based on thin amorphous carbon foil [24–26]. However, the potential for improvement still exists, particularly in achieving a constant, stable phase shift. A laser phase plate can apply a stable, controllable phase shift to the transmitted wave, with negligible electron loss or decoherence. The possibility of rapidly changing the phase delay by varying the laser power is an additional advantage.

Free-space manipulation of energetic electrons used in TEM requires very high laser intensity.

Optics EXPRESS

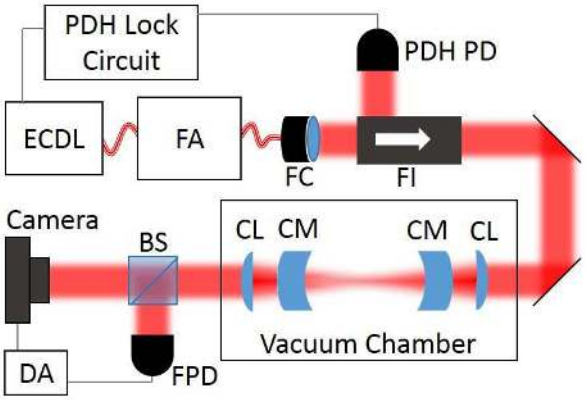

Fig. 1. Schematic diagram of the experimental setup. ECDL = external cavity diode laser, FA = fiber amplifier, FC = fiber coupler, PDH PD = Pound-Drever-Hall lock photodiode, FI = Faraday isolator, CL = coupling lens, CM = cavity mirror, BS = beamsplitter, FPD = fast photodiode, DA = digital data acquisition.

The phase delay induced by a focused Gaussian laser beam can be calculated as

$$\phi = \sqrt{8\pi}\,\frac{\alpha}{\beta\gamma}\,\frac{P}{mc\,\omega^2\,w}\,, \tag{1}$$

where α is the fine structure constant, c is the speed of light, m is the electron mass, β and γ are the electron's relativistic factors, P is the beam power, ω is the laser angular frequency, and w is the beam waist [18]. Another requirement for a ponderomotive phase plate is that the focal spot size should not exceed a few micrometers. According to Eq. (1), imparting a $\frac{\pi}{2}$ phase shift to electrons at a typical TEM energy of 200-300 keV over a distance of several microns necessitates a laser intensity in the range of a few hundred GW/cm^2. Consequently, most experiments with electron scattering on light have been conducted with pulsed laser systems [27]. However, continuous operation is desirable for cryo-EM and other high resolution TEM applications where the signal to noise ratio is the limiting factor [28, 29].

The laser power of a continuous-wave (CW) system can be enhanced using a power build-up cavity. Low-loss cavity mirrors have been shown to withstand intensities up to 0.1 GW/cm^2 [30]. Much higher intensities required for a ponderomotive phase plate can be achieved in a focusing cavity, such as a near-concentric Fabry-Pérot resonator. In this configuration, the fundamental mode has an hourglass shape, with laser power concentrated in a small focal spot at the center but spread out over a large area on the mirror surface, which prevents mirror damage. Tight intra-cavity focusing at low power has been demonstrated in a medium-finesse near-concentric cavity [31]. At the same time, average circulating power of up to 670 kW [32] has been achieved in a focusing cavity built for amplifying trains of ultrashort pulses for intra-cavity high harmonic generation and optical comb spectroscopy in the extreme ultra-violet spectral range [33]. However, a combination of high power and tight intra-cavity focusing necessary for a laser phase plate has not been realized yet.

Here, we demonstrate a high numerical aperture near-concentric cavity with a finesse of $\mathcal{F} > 2.2 \cdot 10^4$ that can be used as a prototype for future development of electron-optical elements based on CW lasers. With 7.5 kW of circulating CW laser power, we reach a maximum intensity of 41 GW/cm^2, previously achieved only in pulsed laser systems. We use numerical simulations to show that with a tenfold further increase of power, the standing-wave phase profile created by the intra-cavity field would be able to function as a nearly ideal Zernike phase plate for a TEM operating at an electron energy of 300 keV.

Optics EXPRESS

2. Experimental Results

Our optical system, shown schematically in Fig. 1, consists of a near-concentric cavity and a CW feeding laser, operating at a wavelength $\lambda = 1064$ nm. The feeding laser comprises an external cavity diode laser, frequency-locked to the cavity using the Pound-Drever-Hall method, and a fiber amplifier. The cavity is designed for insertion into a plane conjugate to the back focal plane of a TEM objective lens, with the electron beam entering the cavity orthogonally to the optical axis. The cavity is formed by two concave mirrors (Layertec) with a diameter of 12.7 mm, radius of curvature of 12.7 mm, and specified reflectivity $\mathcal{R} = 1 - (10 \pm 5) \cdot 10^{-5}$. The back surface of the mirrors is convex, concentric with the front surface. The meniscus shape allows for efficient coupling into the high numerical-aperture mode of the cavity with a single aspheric lens.

The cavity mount allows for adjustment of the tilt and axial position of one of the mirrors, housed in a flexure suspension. Alignment of the near-concentric cavity, requiring angular precision better than 1 μrad, is achieved by three fine-pitched micrometer screws providing rough alignment, pressing against three piezo actuators. The high-power optical module comprising the cavity, the coupling lenses and the mirror alignment optomechanics, is made compact enough to fit into a cylindrical space of 25 mm diameter, which facilitates future integration into a TEM system.

The cavity is suspended in a vacuum chamber pumped down to $2 \cdot 10^{-7}$ mbar, emulating the environment of a TEM column and preventing undesirable ionization of air molecules. Using the tilt and axial motion degrees of freedom of one of the mirrors, the cavity was brought to a near-concentric configuration. To characterize the size of the focal point inside the cavity, we tuned the laser frequency to oscillate around the fundamental mode of the cavity. The transmitted beam was collimated by an aspheric lens (focal length 25 mm) and directed into a CMOS image sensor. Fitting the mode image with a two-dimensional Gaussian profile, we obtain the width of the fundamental mode at the far field, reciprocal to the size of the focal spot. The image, shown in Fig. 2, exhibits a small degree of ellipticity determined by a very slight astigmatism of the cavity mirrors. The two principal axes of the ellipse correspond to numerical apertures of $\mathrm{NA}_a = 0.0469 \pm 0.0005$ and $\mathrm{NA}_b = 0.0524 \pm 0.0005$. The mode waist corresponding to NA_b is $s = \lambda\,(\pi \mathrm{NA})^{-1} = 6.46\,\mu$m.

The reflectivity of the cavity mirrors was measured using the cavity ring-down (CRD) method [34], in which light is briefly injected into the cavity and the subsequent rise and decay in the power of the transmitted light is observed. The injection of light into the cavity was accomplished by rapidly sweeping the laser frequency across a longitudinal mode resonance of the cavity's TEM_{00} mode (rapidly-swept cw-CRD) [35].

Under these conditions, the transmitted electric field amplitude is well-modeled by the inverse Fourier transform of the product of the cavity's transfer function and the spectrum of a linearly-chirped laser field, so that the transmitted power is

$$P(t) \propto \left| \int_{-\infty}^{\infty} d\omega\, e^{i\omega t} \cdot \left[\frac{e^{-i\omega L/c}}{1 - \mathcal{R} e^{-2i\omega L/c}} \right] \cdot \left[e^{-i\omega^2/2\eta} \right] \right|^2 \tag{2}$$

where $\mathcal{R}$ is the cavity mirror reflectance, L is the cavity length, and η is the frequency sweep rate. This model was used to fit the experimentally measured CRD profiles, with $\mathcal{R}$ serving as the fit parameter of interest.

The measured CRD profile is shown in Fig. 2 along with its least-squares best fit to the model described by Eq. (2). Expressing the cavity mirror reflectivity in terms of the cavity mirror transmission, T, and loss, L, such that $\mathcal{R} = 1 - (T + L)$, the fitted profile corresponds to a cavity mirror transmission-plus-loss of 137.9 ± 0.4 ppm. This corresponds to a cavity finesse of $\mathcal{F} = \frac{\pi \mathcal{R}}{1-\mathcal{R}} \approx \frac{\pi}{T+L} = 22780 \pm 65$.

The seed laser was locked to the cavity using the Pound-Drever-Hall method, with side bands generated by direct RF modulation of the seed laser current. The reflected beam was separated by

Optics EXPRESS

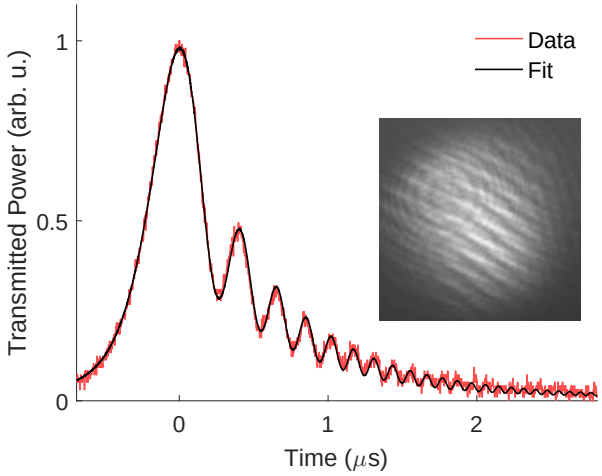

Fig. 2. **Axes:** The cavity ring-down profile (red), and fit to the model described by Eq. (2) (black). The fit corresponds to a cavity mirror transmission-plus-loss of 137.9 ± 0.4 ppm. **Inset:** The mode for which the displayed CRD profile was measured. Fringes are an imaging artifact due to interference from the camera's protective window.

a Faraday isolator and directed into a photodiode. The RF signal from the diode was demodulated and used as the error signal.

To estimate the circulating power in the cavity, in addition to cavity finesse we need to know the coupling efficiency and the transmission-to-loss ratio of the mirrors. Both parameters can be inferred from measurements of the cavity transmission coefficient T_{cav} and reflection coefficient R_{cav}. Denoting the mode overlap between the input beam and the fundamental cavity mode as Q, we have:

$$T_{cav} = |Q|^2 \left(\frac{T}{T+L}\right)^2, \quad R_{cav} = 1 - 2\,|Q|^2 \frac{T}{T+L} + T_{cav} \tag{3}$$

With the laser frequency locked to the cavity resonance, we measured $R_{cav} = 0.34 \pm 0.03$, $T_{cav} = 0.32 \pm 0.03$. Extracting the cavity parameters, we get $|Q|^2 = 0.75 \pm 0.05$ and $\frac{T}{T+L} = 0.65 \pm 0.05$. Taken together with the CRD data, these parameters allow us to determine the mirror transmission $T = 90 \pm 7$ ppm and the amplification factor as $M = |Q|^2 \frac{T}{(T+L)^2} = (T_{cav} + 1 - R_{cav})/(2(T+L)) = 3600 \pm 150$.

With the cavity parameters determined, we proceeded to increase the input power. With the cavity chamber held at atmospheric pressure, increasing the input power beyond 300 mW did not lead to further increase in transmitted power, apparently due to the onset of nonlinear optical effects in air at a circulating power of about 1kW, corresponding to a maximum intensity of 5.5 GW/cm^2. With the chamber evacuated, we were able to reach intra-cavity power of up to 7.5 ± 0.6 kW. The intra-cavity circulating power (inferred from transmitted power) as a function of input power is shown in Fig. 3. The graph is almost linear, with a small deviation at higher power possibly arising due to thermally induced deformations of the cavity housing modifying the cavity alignment. The maximum power was limited by the concern over the risk of thermal damage to the mirrors, which were not well thermally coupled to the mount. With the mode parameters measured above, the maximum measured power corresponds to a maximum intensity of $(41 \pm 4)\,\mathrm{GW/cm^2}$, which would lead to a phase retardation of 0.16 rad for a 300 keV electron beam, or 1.0 rad for a 10 keV beam. Repeated CRD measurements at low power confirmed that no damage to the mirrors occurred during the high power run.

Optics EXPRESS

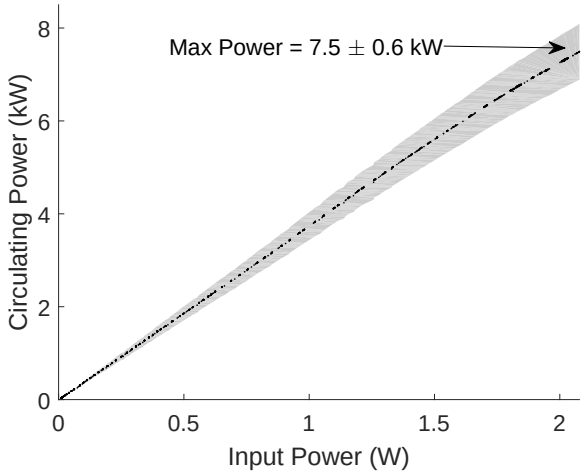

Fig. 3. Intra-cavity circulating power as a function of input power. The gray region represents the 68% confidence interval. The circulating power is determined via the measurement of the amplification factor $M = (T_{cav} + 1 - R_{cav})/2(T + L)$. Here, T_{cav} was monitored as a function of input power by simultaneously measuring the input power (using a calibrated partially-reflective window) and the transmitted power. R_{cav} was measured once at low power.

3. Numerical Modeling

To evaluate the effect of the laser phase plate on TEM of biological macromolecules, we have conducted numerical simulations of TEM imaging of human hemoglobin embedded in vitreous ice. This tetrameric complex has a molecular mass of approximately 64 kDa, which is too small for conventional TEM reconstruction, but has been recently solved to 3.2 Å resolution using phase contrast TEM with a carbon foil phase plate [36].

Multislice simulations were performed using the methods and potentials described in Kirkland [37]. An accelerating voltage of 300 kV, a pixel size of 0.2 Å, an effective focal length of 20 mm, and spherical aberration of 1.3 mm was used. Because shot noise and thermal smearing of the potentials dominated the information limit of the simulations, the finite spatial and temporal coherence of the electron beam were neglected in the simulations. The hemoglobin structure used was downloaded from the protein databank [38]. The thermal vibration of the protein atoms was assumed to be 0.1 Å, applied as an envelope function. The continuum model of vitreous ice developed by Shang and Sigworth [39] was used to model the embedding potential around the hemoglobin structure, numerically integrated in 3D.

The results of the modeling are presented in Fig. 4. The ribbon model of the ring-like protein complex is shown in Fig. 4 (a). Simulated images of hemoglobin, seen in the same projection as Fig. 4 (a) are shown in Figs. 4(b) and 4(c). Highly transparent biological macromolecules are conventionally made visible by defocusing the imaging system from the specimen plane, creating a phase contrast image with an oscillatory contrast transfer function [22]. While a higher defocus results in higher contrast at low spatial frequencies, it also leads to a loss of contrast at high spatial frequencies. The defocus of 1 μm used in Fig. 4(b) is a value that still allows for reconstruction of density maps with near-atomic resolution [40, 41]. The shot noise is modeled assuming an effective dose of 20 $e/Å^2$, typically used in TEM protein structure studies as an optimum point between radiation damage, which increases with a higher dose, and the shot noise, which decreases with a higher dose. Figure 4(c) shows an in-focus image of hemoglobin with

Optics EXPRESS

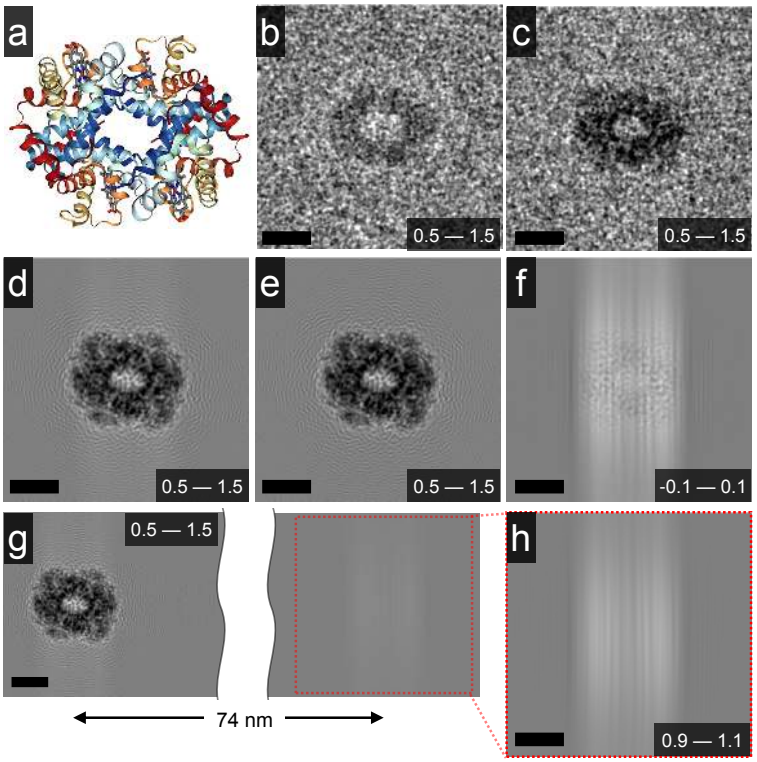

Fig. 4. Modeling of TEM images of a hemoglobin molecule with a cavity-based ponderomotive phase plate: (a) ribbon plot of the hemoglobin molecule; (b) a TEM image of the molecule embedded in 30 nm of vitreous ice, electron energy 300 keV, underfocus 1 μm, dose 20 e/Å^2; (c) in-focus phase contrast image with a laser-based phase plate, same conditions; (d) an image of the same molecule with the cavity-based phase plate, in focus and without noise; (e) similar image with an 'ideal' phase plate; (f) the difference between (d) and (e), shown with enhanced contrast for visibility; (g) a hemoglobin image (left part of the panel) and a first-order weak ghost image appearing on the right; (h) the ghost image shown with enhanced contrast. The limits of the gray-scale map are shown in the corner of each image. All scale bars are 2nm. The cavity numerical aperture in the model is $NA = 0.05$, in agreement with the experimentally demonstrated parameters. The model assumes that the intra-cavity power is scaled to achieve full $\frac{\pi}{2}$ retardation at maximum, which requires a roughly tenfold further increase of optical power.

Optics EXPRESS

the ponderomotive phase plate at the same electron dose. A full $\pi/2$ phase shift at the intensity maximum is assumed. The phase contrast image demonstrates a stronger signal at low spatial frequencies compared to a defocus-contrast image, which is expected to enable particle projection classification and alignment for macromolecules at least as small as hemoglobin.

Figure 4(d) shows the image from Fig. 4(c) simulated without shot noise. For comparison, a noise-free in-focus image using an 'ideal' phase plate is shown in Fig. 4(e). The difference between the two images is shown with enhanced contrast in Fig. 4(f), illustrating the effect of the anisotropic structure of the standing wave used in the ponderomotive phase plate.

A side effect of passing an electron beam through a standing laser wave is that the standing wave acts as a diffraction grating for the electrons, which generates additional weak 'ghost' images. These ghost images are displaced from the primary image by a distance $\delta x = 2nf\lambda_e/\lambda$, where n is the diffraction order, f is the focal distance of the TEM objective and λ_e is the electron wavelength. A first order ghost image is shown on the right side of Fig. 4(g), and again with enhanced contrast in Fig. 4(h). These panels are shown without the shot noise, which would otherwise render the ghost image nearly invisible. Since the amplitude of such ghost images is well below shot noise, they will not be visible in individual images, and will amount to an inconsequential contribution to the noise in the averaged images used for density map reconstruction.

4. Outlook

The numerical results shown in Fig. 4 demonstrate that a standing wave built up in a focusing resonator creates a contrast transfer function suitable for phase contrast imaging. Importantly, the well-defined spatial structure of the cavity mode ensures that the contrast transfer function can be accurately taken into account when interpreting the EM images. While the intensity demonstrated in our experiment is about an order of magnitude below that required to impart a $\frac{\pi}{2}$ phase shift to a 300 keV electron beam, it may be sufficient for the initial demonstration of the ponderomotive retardation. Furthermore, using state of the art mirrors it should be possible to increase the cavity finesse to $2 \cdot 10^5$. Increasing the input power to 30 W, which is possible with commercial fiber amplifiers at NIR wavelength, should be sufficient to increase the focal intensity to well beyond 10^{12} W/cm^2.

In this work, we have focused on developing a laser-based Zernike phase plate. However, a number of other tools can be envisioned using high-intensity intra-cavity CW laser fields. For example, a quantum imaging method based on an interaction-free measurement scheme has been proposed [42]. A significant obstacle to implementing this scheme lies in the absence of a high quality beam splitter for the electron wave function. A CW standing wave inside an optical cavity can act as a highly regular, virtually lossless phase grating, coherently splitting an electron beam into two paths via Kapitza-Dirac scattering in the Bragg regime [16]. Such a beam splitter could also enable various electron interferometry schemes, mimicking the diverse family of optical interferometers used for metrology and sensing.

Finally, we note that the type of cavity we have built can be of interest to a wide class of experiments. The combination of a small mode volume with the open, accessible geometry of a high-NA near-concentric resonator can be useful for cavity QED experiments [43, 44]. Furthermore, the ability to build up very high circulating power can be used to implement ultra-deep dipole traps [45, 46], as well as for trapping and cooling nanoparticles [47–49].

In summary, we have developed a high-finesse optical cavity with a tightly focused fundamental mode. We verified by numeric simulations that such field configuration can function as a ponderomotive phase plate for TEM. We have demonstrated that optical intensity in the range of tens of GW/cm^2 can be reached in a CW laser system using a near-concentric Fabry-Pérot resonator. These results represent a significant step towards ponderomotive phase contrast TEM, and, more generally, pave the way towards laser based coherent control of free space electron

Optics EXPRESS

wave functions.

Funding

This material is based upon work supported by the National Science Foundation under Grant No. 1040543. OS was supported by a Human Frontier Science Program postdoctoral fellowship LT000844/2016-C. PH thanks the Austrian Science Fund (FWF): J3680. Work at the Molecular Foundry was supported by the Office of Science, Office of Basic Energy Sciences, of the U.S. Department of Energy under Contract No. DE-AC02-05CH11231.